

Image Reconstruction from Data Collected with an Imaging Interferometer

Zachary J. DeSantis

Sam T. Thurman

Troy T. Hix

Chad E. Ogden

Lockheed Martin Space Systems Company

ABSTRACT

The intensity distribution of an incoherent source and the spatial coherence function at some distance away are related by a Fourier transform, via the Van Cittert-Zernike theorem. Imaging interferometers measure the spatial coherence of light propagated from the incoherently illuminated object by combining light from spatially separated points to measure interference fringes. The contrast and phase of the fringe are the amplitude and phase of a Fourier component of the source's intensity distribution. The Fiber-Coupled Interferometer (FCI) testbed is a visible light, lab-based imaging interferometer designed to test aspects of an envisioned ground-based interferometer for imaging geosynchronous satellites. The front half of the FCI testbed consists of the scene projection optics, which includes an incoherently backlit scene, located at the focus of a 1 m aperture $f/100$ telescope. The projected light was collected by the back half of the FCI testbed. The collection optics consisted of three 11 mm aperture fiber-coupled telescopes. Light in the fibers was combined pairwise and dispersed onto a sensor to measure the interference fringe as a function of wavelength, which produces a radial spoke of measurements in the Fourier domain. The visibility function was sampled throughout the Fourier domain by recording fringe data at many different scene rotations and collection telescope separations. Our image reconstruction algorithm successfully produced images for the three scenes we tested: asymmetric pair of pinholes, U.S. Air Force resolution bar target, and satellite scene. The bar target reconstruction shows detail and resolution near the predicted resolution limit.

This research was developed with funding from the Defense Advanced Research Projects Agency (DARPA). The views, opinions and/or findings expressed are those of the author(s) and should not be interpreted as reflecting the official views or policies of the Department of Defense or the U.S. Government.

1. INTRODUCTION

The Fiber Combined Interferometer (FCI) testbed was created as part of the DARPA Galileo program, a study on ground-based interferometry for imaging satellites in geostationary orbit. FCI was constructed using fiber-coupled receiver telescopes to transport light to a central pupil-plane beam combiner. The light was then transported to a spectrograph where spectra modulated by interference fringes were observed. We measured fringes for many baseline lengths and orientations to reconstruct an image of the object. This method of imaging is a form of Michelson-stellar interferometry, based on the Van Cittert-Zernike theorem [1], which relates the object's normalized intensity distribution, $\bar{I}(\xi; \lambda)$, in a plane a distance, z , away, to the complex coherence factor, μ , with a Fourier transform,

$$\mu(\rho_1, \rho_2; \lambda) = e^{-i\Psi} \iint_{-\infty}^{\infty} \bar{I}(\xi; \lambda) e^{i\frac{2\pi}{\lambda z}(\rho_2 - \rho_1) \cdot \xi} d^2\xi, \quad (1.1)$$

where λ is the wavelength of light,

$$\Psi = \frac{\pi}{\lambda z} (\boldsymbol{\rho}_2^2 - \boldsymbol{\rho}_1^2), \quad (1.2)$$

$\bar{I}(\boldsymbol{\xi}; \lambda)$ is defined as

$$\bar{I}(\boldsymbol{\xi}; \lambda) = \frac{I(\boldsymbol{\xi}; \lambda)}{\iint_{-\infty}^{\infty} I(\boldsymbol{\xi}'; \lambda) d^2 \boldsymbol{\xi}'}, \quad (1.3)$$

where $I(\boldsymbol{\xi}; \lambda)$ is the object's intensity distribution, and $\boldsymbol{\rho}_1$ and $\boldsymbol{\rho}_2$ are the 2-D spatial projections onto the plane perpendicular to the line of sight of the coordinates of the telescopes used to collect the light. Often the phase term, $e^{-i\Psi}$, is neglected because it vanishes for several conditions [1]. If the distance is sufficiently large the term will vanish. If the collection telescopes always lie on a reference sphere with radius z , centered on the object, the phase term will vanish. A symmetric placement, relative to the optical axis of the telescopes ($\boldsymbol{\rho}_2 = -\boldsymbol{\rho}_1$), effectively cancels the phase term. Lastly, the term can be accounted for by knowing the telescope geometry, relative to other baseline measurements. For the FCI testbed, the object is in the focal plane of a projection telescope, which effectively cancels the phase term.

The light collected by the telescopes is brought together and interfered to produce a fringe. The amplitude and phase of the fringe give the complex visibility, V , at a Fourier location given by

$$\mathbf{u} = (u, v) = \frac{\boldsymbol{\rho}_2 - \boldsymbol{\rho}_1}{\lambda z} = \frac{\mathbf{B}}{\lambda z}, \quad (1.4)$$

where \mathbf{B} is the telescope vector separation or baseline. The baseline is also commonly expressed in terms of the separation distance, $|\mathbf{B}|$, and the azimuthal angle.

Ideally, all Fourier components would be measured and synthesized to form an image of the object; however, measuring every Fourier component on a Cartesian grid is a lengthy process. Every new position requires movement and realignment of at least one telescope.

To help measure different radial regions of the Fourier domain, multiple spectral channels can be added. For simplicity, we will assume the gray world approximation [2], which assumes each point on the object has the same spectrum, or $\bar{I}(\boldsymbol{\xi}; \lambda) = A(\lambda) \bar{I}(\boldsymbol{\xi})$, where A is the spectrum, independent of the location in the object field. For a single wavelength, each fringe measurement gives a single Fourier component of \bar{I} . The Fourier coordinates from Eq. (1.4) scale inversely with wavelength. For a fixed telescope baseline, each spectral channel occupies a different region of the Fourier domain. Measuring the visibility for each channel simultaneously gives a radial spoke of measurements in the Fourier domain. The length of the spoke is proportional to both the baseline length and the bandwidth. Because the maximum wavelength is finite, the spoke does not extend to the origin. For a given angle, multiple baseline lengths are required to fill out a spoke from the origin (the shortest baselines are difficult to collect because there are physical constraints preventing telescopes being too close to each other like housings and support structures) to the maximum desired spatial frequency. Eq. (1.4) is used to relate the maximum desired spatial frequency (roughly the inverse of the system resolution) to the system parameters. Under the gray-world approximation, every

measurement in the spoke is a Fourier component of the same normalized intensity distribution. This assumption allows us to easily populate the Fourier domain with spokes of measurements, while avoiding the time cost of movement and alignment of the telescope for each radial point on the spoke.

For a real system, in addition to non-uniform sampling, there is a corruption of phase information due to atmospheric turbulence. For our lab system, the atmosphere is significantly more benign, but there is still atmospheric variation and mechanical vibration amongst other path length errors that require a fringe tracking algorithm to estimate optical path difference fluctuations over time. Closure phase is a common method to measure partial phase information. However, we expect the object to be very dim in a real system, and the closure phase would be too noisy to be practical.

An additional technique is desirable to quickly fill the Fourier domain with measurements that also gives a phase relation. Because one can measure the wavelengths simultaneously, the atmospheric relative piston error (in units of physical length) between the two telescopes is the same for the measurements at all the wavelengths for a given \mathbf{B} . To first order, the difference in path length, L , between the two telescopes will cause a piston phase error for the longest wavelength, λ_{\max} , of

$$\varphi_e = \frac{2\pi L}{\lambda_{\max}} = \frac{2\pi\nu_{\min} L}{c}, \quad (1.5)$$

where c is the speed of light and ν_{\min} is the smallest optical frequency of the spectral channels. If we assume the spectral channels are equally spaced in optical frequency with spacing $\Delta\nu$, the piston error for the n th spectral channel, having frequency $\nu_{\min} + n\Delta\nu$, is

$$\varphi_e(n) = \frac{2\pi(\nu_{\min} + n\Delta\nu)L}{c}. \quad (1.6)$$

Since the measurements for all spectral channels for a given baseline are made simultaneously, L is the same for each channel in the spoke, making the piston error equivalent to a linear phase error (in n) across the entire spoke. In addition to the gray-world assumption, this method also currently assumes that we know and compensate for the dispersion in the atmosphere and system. For the FCI testbed, compensator plates are used in the beam combiners to correct the errors due to different amounts of dispersion between the two arms of the interferometer. Hence, the data sets we will consider are non-uniformly spaced on a non-Cartesian grid, with spoke-to-spoke linear phase errors and will require an image reconstruction algorithm to form a high-resolution image.

For the number of spectral channels for each telescope separation, just one unknown exists in the data. Using such a measurement scheme populates the Fourier domain with spokes of measurements with the correct phase information except for one unknown linear term for each spoke. Since the data is sparse, non-uniformly spaced, and has phase errors, the need for an image reconstruction algorithm is clear. We developed an image reconstruction algorithm and have previously demonstrated its success in simulation [3-5]. In this paper, we demonstrate successful image reconstructions from experimental data.

2. EXPERIMENTAL SETUP

A diagram of the FCI testbed is shown in Fig. 1 below. The testbed is composed of three fiber-coupled receiver telescopes which are each split and then combined pairwise in three Michelson (pupil-plane) interferometers. The

broadband output beams of all three combiners are arranged into a vertical stack of six beams. The output beams all pass through a prism and focusing lens, to form six spectra on an EMCCD camera.

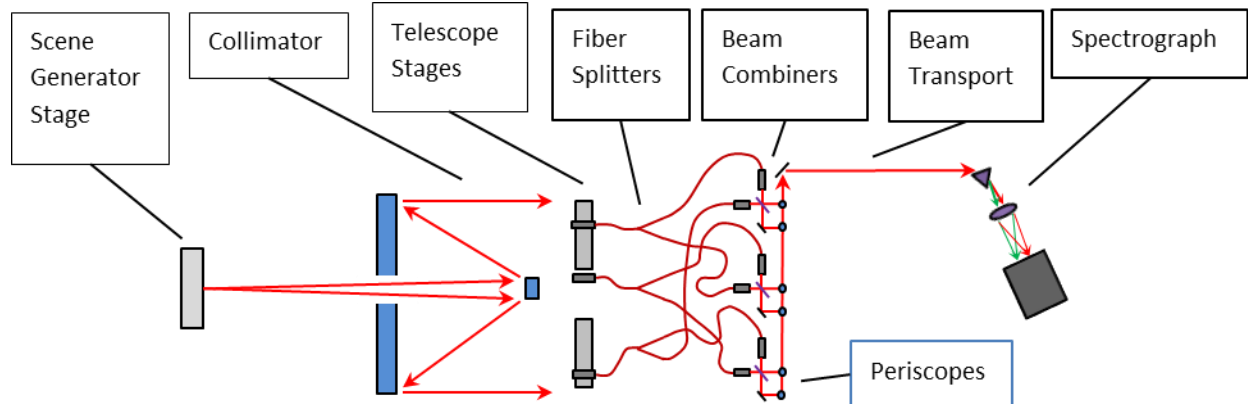


Fig. 1. Schematic layout of the FCI testbed. Light from the Scene Generator is collimated, then collected by the fiber-coupled receiver telescopes. Each fiber is split into two outputs, then fed into one of three pupil-plane 2-beam combiners. All output beams are arranged into a vertical stack and are imaged through the spectrograph, forming a stack of six spectra on the camera which are modulated by interference fringes.

Each functional part of the testbed is described below in more detail. The order of components follows photon flow from light source to detector.

1. Scene Generator - The scene generator consists of, in addition to several calibration sources, the target illuminated with spatially incoherent light. The extended scene illuminator is made spatially incoherent by illuminating a pair of diffusers in series, each followed by a glass light pipe.
2. Collimator - Light emitted by the scene generator is collimated by a 1-meter diameter f/100 telescope. The long f-number is useful because it allows the scene objects to be macroscopically sized. Scene slides can be made relatively inexpensively with 25 μm pixels that have 256 greyscale levels, and those pixels will be unresolved by more than a factor of 2 using the full 1 m aperture. Fig. 2 below conveys the extremely small 53 μrad angle of the 5.3 mm satellite scene viewed through the collimator.
3. Telescope Stages - The sparse aperture consists of three 11 mm aperture telescopes which can be moved transverse to the beam line and pointed (via tip/tilt) such that they couple the light from the source into a 780 nm polarization maintaining (PM) optical fiber. The fiber tip is held near the focus of the lens in an x/y mount such that the fiber tip can be fine-tuned in a plane normal to the optical axis.
4. Fiber Splitters - 2-meter long 780 nm PM fiber pigtailed lead from the receiver telescopes to the fiber switchyard. They couple into custom broadband free space 1x2 splitters made by Micro-optics, which split the light approximately 50/50 into two PM output fibers. The splitter outputs couple to 2-meter long PM fiber pigtailed that feed collimator telescopes in the beam combiner.
5. Beam Combiners - The telescopes are combined in pairs, once with each neighbor; Beam Combiner 1 (BC1) mixes telescope T2 with T3, BC2 mixes T1 with T3, and BC3 mixes T1 with T2. The combiner produces two output beams, with fringes 180 degrees out of phase from each other, each output beam containing approximately half of the input light from each telescope
6. Beam Transport - The beam combiners produce a total of six output beams, which are spatially separated with periscopes and directed downstream to the spectrograph.
7. Spectrograph - Fringes are dispersed onto the EMCCD, measuring the 6 sets of fringes (2 for each of 3 baseline pairs) on different parts of the sensor. A sample fringe is shown in Fig. 3.

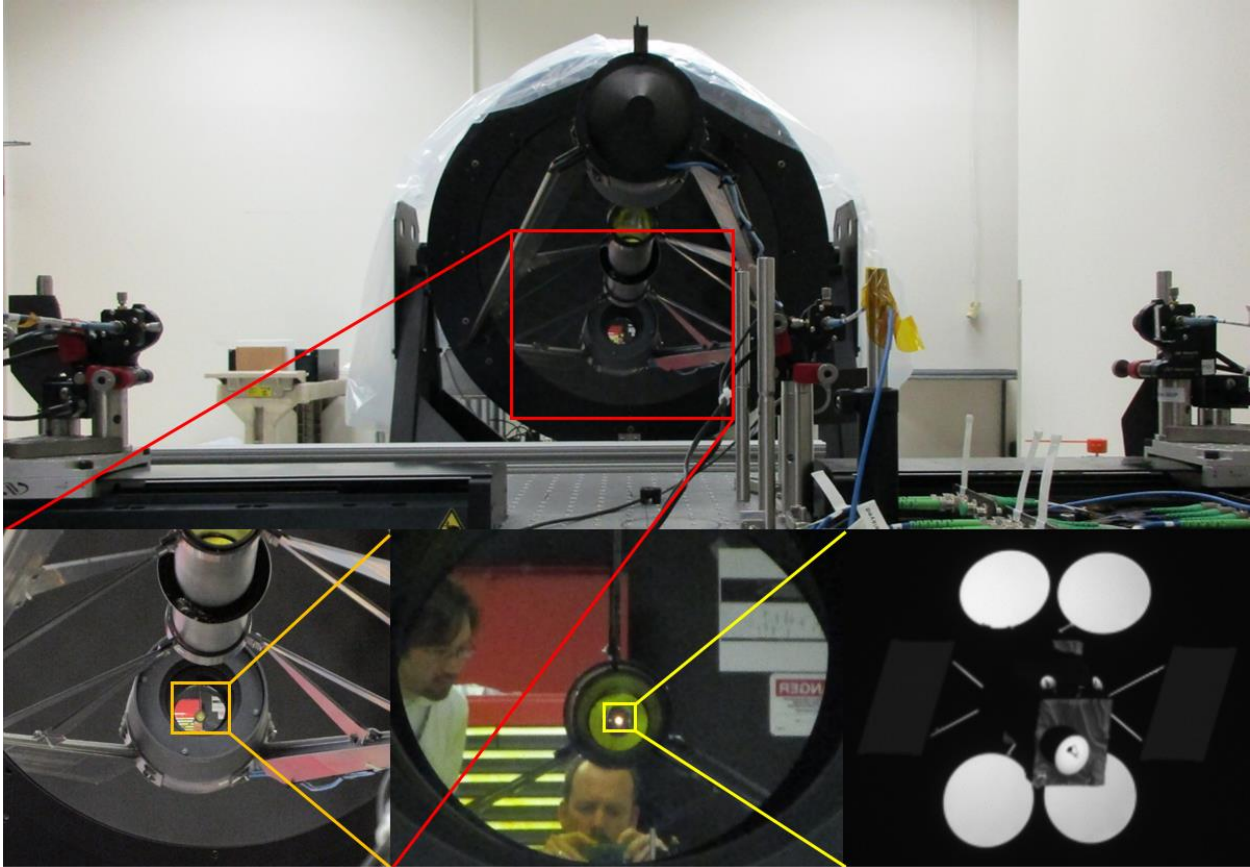


Fig. 2. Scene as viewed through the Collimator. The 5.3 mm diameter target, seen through the 100m focal length collimator subtends an angle of $53 \mu\text{rad}$.

3. FRINGE DATA REDUCTION

Before the visibility can be extracted from the measured fringe data, the fringes need to be calibrated. A spectral calibration source is used to identify the pixel-to-wavelength mapping for each of the 6 fringe patterns.

Each fringe also needs to be calibrated to account for system visibility. An ideal system has a system visibility equal to unity (i.e. with an ideal point source, all fringes should have perfect contrast at all wavelengths). System visibilities are reduced by scattering, stray light, polarization mismatch, and residual unmatched dispersion in the fibers. To account for system visibilities, we measure the interference fringes from an unresolved point source. Each fringe from the point source needs a wavelength dependent photometric calibration. To determine the photometric calibration, we apply labels to identify each light path through the beam combiner, $(a_{i\alpha}, a_{i\beta}, b_{i\alpha}, b_{i\beta}, c_{i\alpha}, c_{i\beta})$, as in Fig. 4. The two beam interference between the input light, I_A , I_B , and I_C , through all six paths can be written as

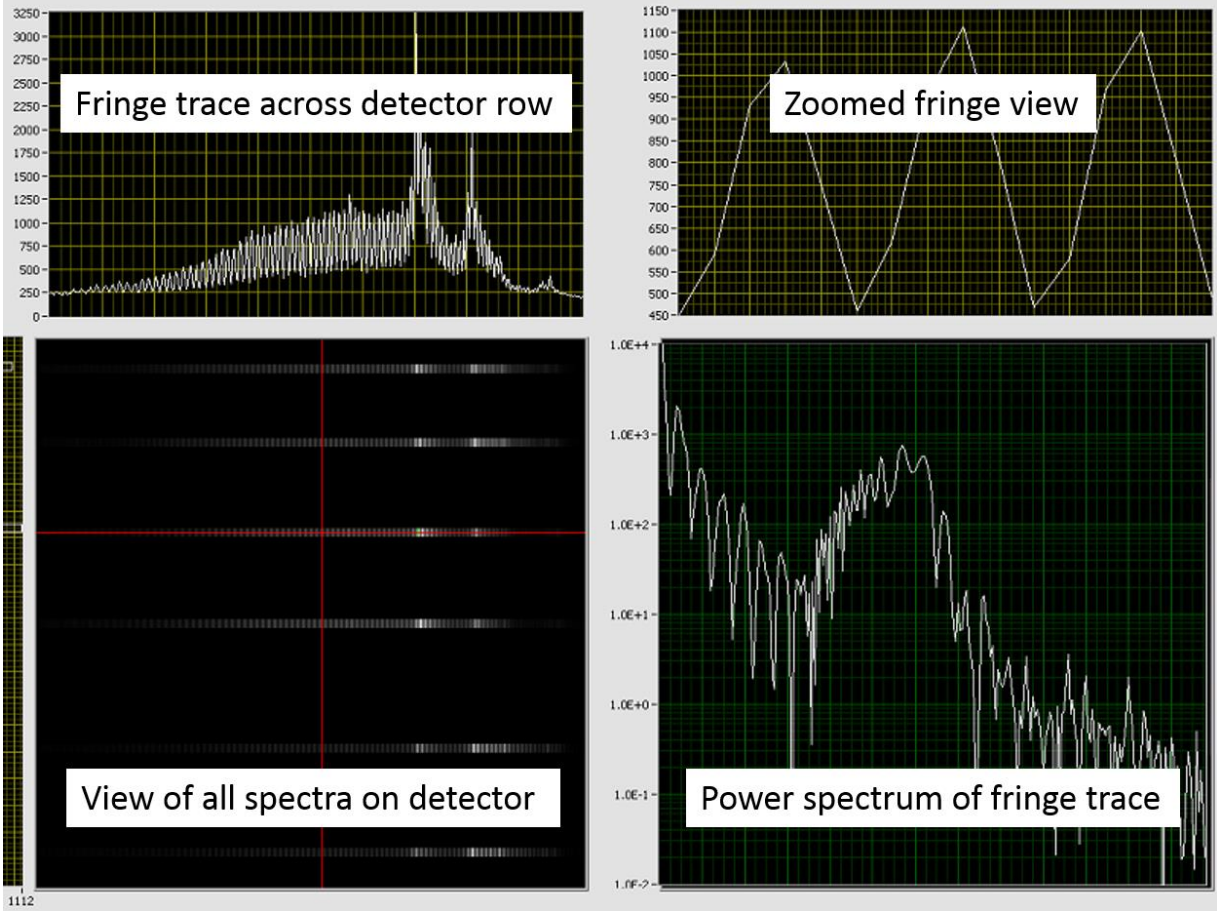


Fig. 3. Interference fringes on detector.

$$\begin{pmatrix} I_{1\alpha} \\ I_{1\beta} \\ I_{2\alpha} \\ I_{2\beta} \\ I_{3\alpha} \\ I_{3\beta} \end{pmatrix} = \begin{pmatrix} 0 & b_{1\alpha} & c_{1\alpha} & 2\sqrt{b_{1\alpha}c_{1\alpha}} & 0 & 0 \\ 0 & b_{1\beta} & c_{1\beta} & -2\sqrt{b_{1\beta}c_{1\beta}} & 0 & 0 \\ a_{2\alpha} & 0 & c_{2\alpha} & 0 & 2\sqrt{a_{2\alpha}c_{2\alpha}} & 0 \\ a_{2\beta} & 0 & c_{2\beta} & 0 & -2\sqrt{a_{2\beta}c_{2\beta}} & 0 \\ a_{3\alpha} & b_{3\alpha} & 0 & 0 & 0 & 2\sqrt{a_{3\alpha}b_{3\alpha}} \\ a_{3\beta} & b_{3\beta} & 0 & 0 & 0 & -2\sqrt{a_{3\beta}b_{3\beta}} \end{pmatrix} \begin{pmatrix} I_A \\ I_B \\ I_C \\ |V_1|\sqrt{I_B I_C} \cos \phi_1 \\ |V_2|\sqrt{I_A I_C} \cos \phi_2 \\ |V_3|\sqrt{I_A I_B} \cos \phi_3 \end{pmatrix} \quad (1.7)$$

where the $|V_i|$ are the photometrically calibrated fringe amplitudes and the ϕ_i are the fringe phases for each of the three baseline pairs, and the left hand intensities are the measured outputs at each of the six paths. To determine the throughputs of the individual beam paths, light is collected with each telescope individually. This solves for all 6 throughput values necessary to build the matrix in the center. Having the center matrix values, collection the fringes from all six outputs produces the left hand side. A matrix inversion and multiply then solves for the right hand vector, from which we can solve for $|V_i| \cos \phi_i$, which is the normalized fringe. Finally, to increase SNR, the normalized fringes are tracked and coherently integrated. The magnitude and phase are then extracted from the fringe giving the complex Fourier measurement. This is done for all spectral frequencies. Because our point source is actually a pinhole of finite size, the last step to calculate the system visibility is to divide by the theoretical visibility from a pinhole.

To extract object fringes, the same spectral calibration and photometric calibration procedures are performed with the additional step of dividing the resulting object data by the system visibility calculated from the pinhole source. The data contains the linear phase errors from Eq. (1.6).

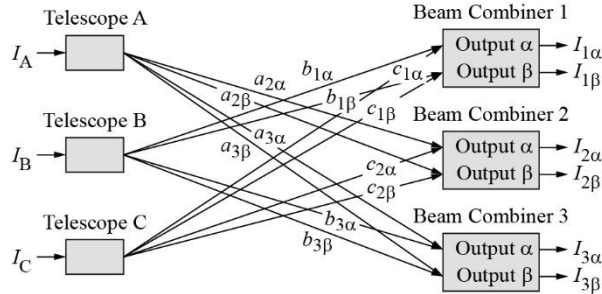


Fig. 4. Beam path labeling through beam combiner.

4. IMAGE RECONSTRUCTION ALGORITHM

The image reconstruction algorithm consists of 4 parts [3-5]: autocorrelation retrieval, support estimation, linear phase estimation, and a final image optimization. There is overlap and repetition of these four parts, where the object support, linear phase correction terms, and image reconstruction estimates are repeatedly updated during the process in a low to high resolution bootstrapping approach.

After the Fourier data is extracted from the fringe, the first step of the image reconstruction algorithm is autocorrelation retrieval. The purpose of autocorrelation retrieval is to eventually build an estimate of the object support from the retrieved autocorrelation. From the autocorrelation theorem [1], only the squared magnitude of the Fourier data is required to reconstruct an autocorrelation. Because this step only uses the square of the magnitude of the Fourier data, any phase errors in the data do not affect the reconstruction. The reconstruction process uses an iterative transform algorithm followed by a nonlinear optimizer that includes the shrinkwrap algorithm [6], to estimate the autocorrelation from the square of the magnitude data.

The shrinkwrap algorithm periodically updates the support estimate during optimization to simultaneously refine the support and recover the image, or, in this case, the autocorrelation. It does this by applying a blur kernel to the object and thresholding. In areas where the intensity estimate is bright, the support estimate will expand, and in areas where the intensity estimate has little energy, the support estimate will shrink.

After we recover an estimate for the autocorrelation, a threshold is applied to produce the autocorrelation support. The autocorrelation support is used with the two-point rule [7, 8] which provides a locator set, which is a rough bound for the underlying object support. This locator set is not perfect because the data we are using is sparse and non-uniform, which makes the autocorrelation retrieval imperfect. The autocorrelation retrieval is performed on data from the shorter baselines.

The support estimate is then refined with additional optimization. This optimization step performs a low-to-mid-resolution bootstrapping process that uses the magnitude of the measured visibility data (amplitude of the data). The bootstrapping process performs a series of reconstructions with increasing resolution by slowly adding in longer

baseline data. This support refinement process, again done with the shrinkwrap algorithm, produces a support much more accurate than the initial estimate out of the autocorrelation retrieval algorithm.

The next step in the algorithm searches for per-spoke linear phase corrections to find the set most consistent with the support estimate while simultaneously forming the image that corresponds to the set of linear phase corrections. We use a least-squares inversion of the non-uniform visibility data to provide the object that gives the best least-squares fit to the data with the current phase correction estimates. The phase error corrections are optimized to minimize a consistency metric and nonnegativity metric. In the process of solving for the phase corrections and the image, we also refine the support estimate further through the use of the shrinkwrap algorithm.

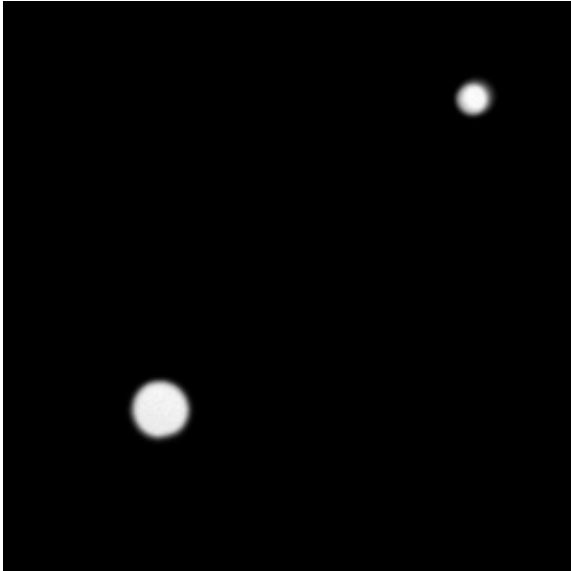
The final stage of the algorithm uses the object estimate and support output from the least squares reconstruction process and performs a final fit. For this stage, we minimize a weighted set of metrics. For all cases, we use a data consistency metric that is invariant to per-spoke linear phase errors and per-spoke scaling [5], a nonnegativity metric, and a support constraint metric. The optimization uses several techniques to move past local minima, like alternating between different forms of an error metric, and filtering out high-frequency artifacts. The output of this last step of the full image reconstruction algorithm is a high-resolution reconstruction and a high-resolution support estimate, again found by using shrinkwrap. The last iteration of the algorithm, we often set the weight of the support constraint to zero to allow the object to expand in areas where the shrinkwrap algorithm shrank too much (dim areas).

5. RESULTS

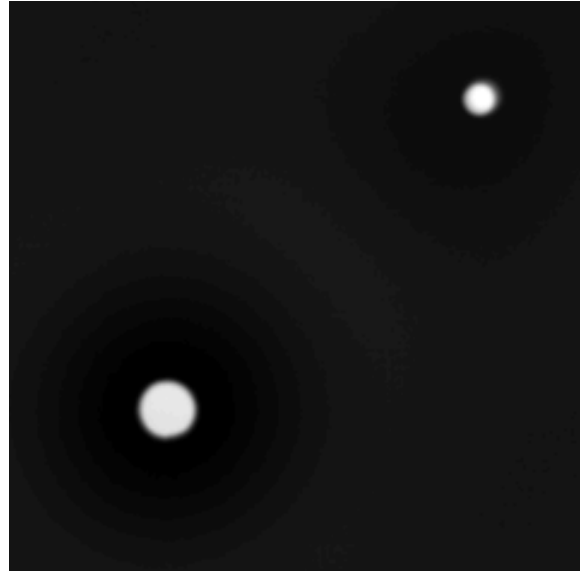
The above algorithm was applied to data collected from three different object scenes. The first object was a pair of pinholes of different diameters. Fig. 5 shows the results for the asymmetric pinhole scene, which consists of (a) the context camera image of the scene, (b) the bandlimited image showing the diffraction-limited resolution corresponding to the Fourier coverage, (c) a dirty image found by applying a priori per-spoke piston and linear phase corrections to the data (found by comparing the data to the context camera image), and (d) a nonlinear reconstruction result which did not use a priori knowledge of any kind. Fig. 6 shows the nonlinear construction with best fit circles. The true (based on measurements with a separate microscope system) diameters of the pin-holes were 0.620 mm and 0.365 mm and the true center-to-center separation was 5.043 mm. Based on the reconstructed image, the diameters of the best fit circles were 0.63 mm for the large hole and 0.37 mm for the small hole, while the separation was 5.05 mm. These values are in an excellent level of agreement with the microscope measurements, considering that diffraction limited resolution is roughly $(0.612 \mu\text{m})(100 \text{ m})/(0.811 \text{ m}) = 75 \mu\text{m}$.

Fig. 7 shows the same as Fig. 5 but with an Air Force Bar Target as the object. Fig. 8 shows a zoom-in on the center of the band-limited image and the nonlinear reconstruction. The cutoff spatial frequency for the minimum wavelength and maximum baseline of the measurements is $(0.810 \text{ m})/(0.612 \mu\text{m})/(100 \text{ m}) = 13.2$ cycles/mm, which corresponds approximately to the Group 3, Element 6 bar set with a spatial frequency of 14.25 line pairs/mm. The nonlinear reconstruction has the same resolution as the band-limited bar target, showing that we reconstructed an image near the ideal resolution limit.

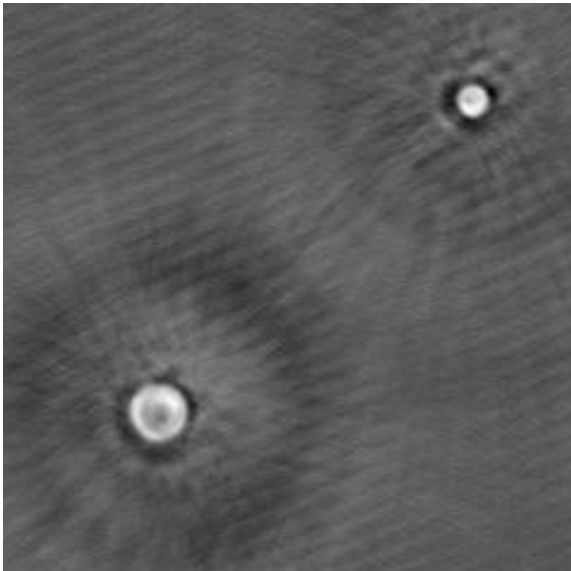
Fig. 9 shows the same as Fig. 5 but for a satellite scene. We are able to capture many of the fine object features in the nonlinear reconstruction. By not using the support metric for the last round of iterations, we were able to recover the faint solar panels on either side of the main bus.



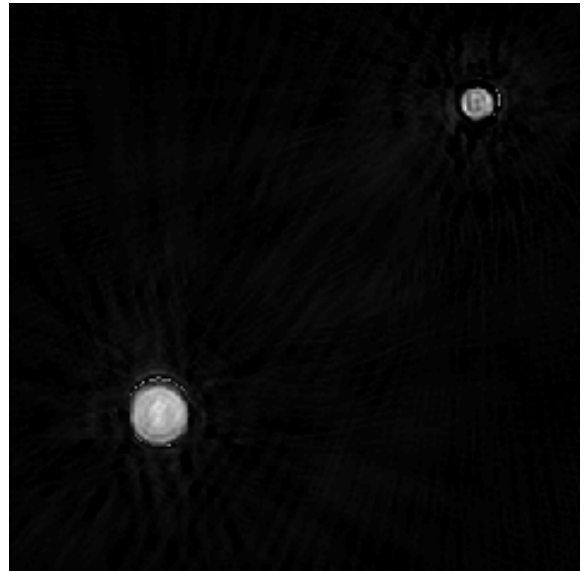
(a)



(b)



(c)



(d)

Fig. 5. Asymmetric Pinholes. (a) Camera image of back-illuminated scene, (b) bandlimited camera image, (c) dirty image using a priori linear phase corrections learned by comparing the data to the true object, and (d) nonlinear reconstruction with no use of a priori knowledge.

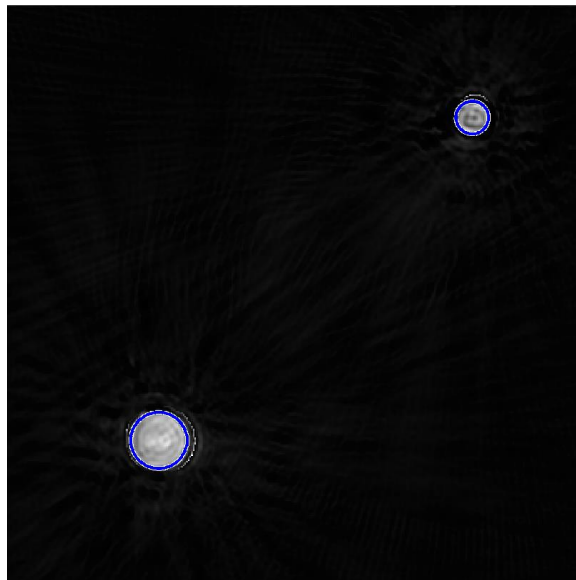
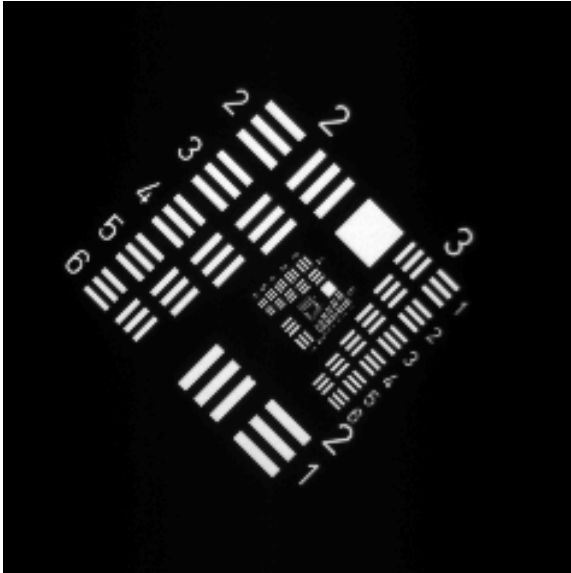
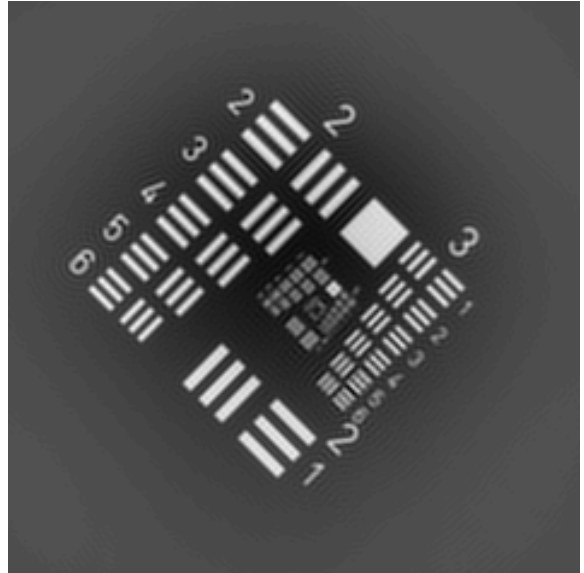


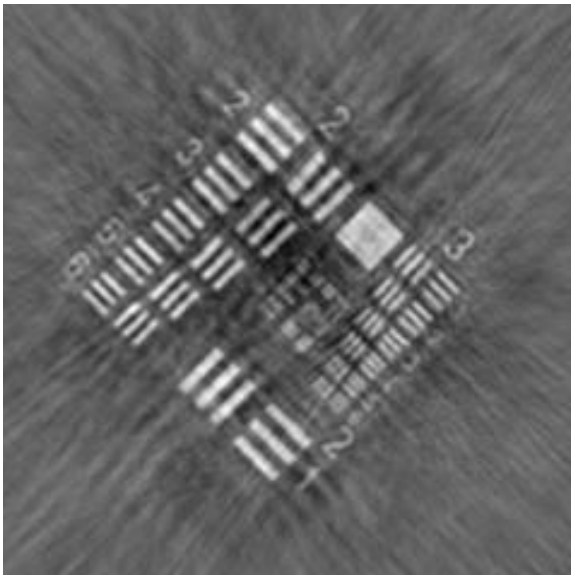
Fig. 6. Measured Asymmetric Binary Reconstruction. Diameter of large hole measured to be 0.63 mm, diameter of small hole measured to be 0.37 mm, and separation measured to be 5.05 mm. Actual values are 0.620 mm and 0.365 mm, separated by 5.043 mm.



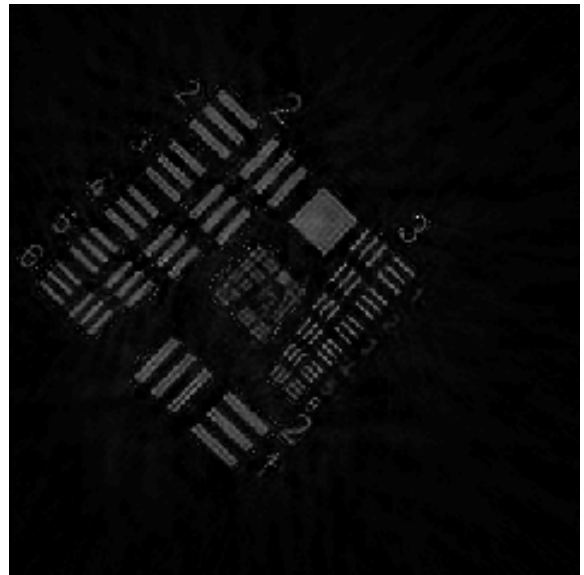
(a)



(b)

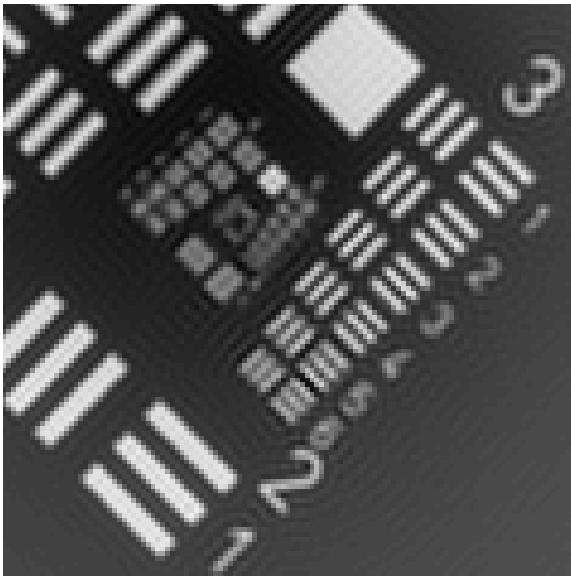


(c)

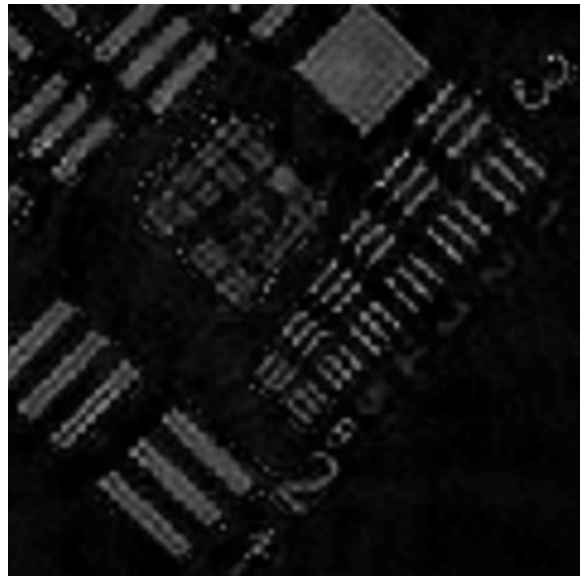


(d)

Fig. 7. Air Force Bar Target. (a) Context camera image of back-illuminated scene, (b) bandlimited camera image, (c) dirty image using a priori phase corrections learned by comparing the data to the true object, and (d) nonlinear reconstruction with no use of a priori knowledge.

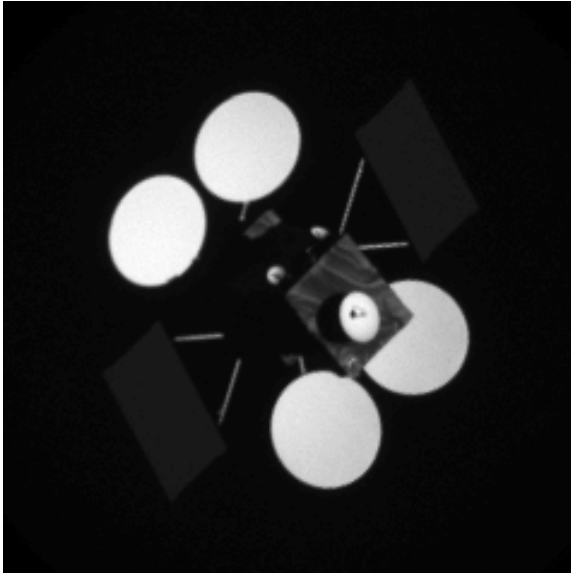


(a)

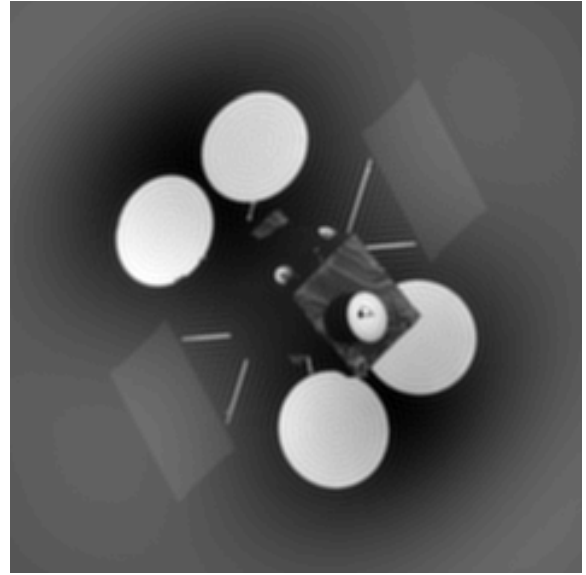


(b)

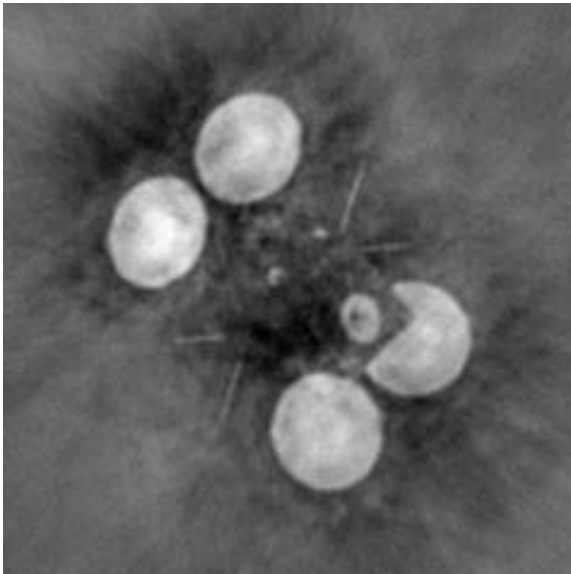
Fig. 8. Air Force Bar Target Zoom. (a) Bandlimited camera image showing fundamental resolution limit and (b) nonlinear reconstruction reaches fundamental resolution limit.



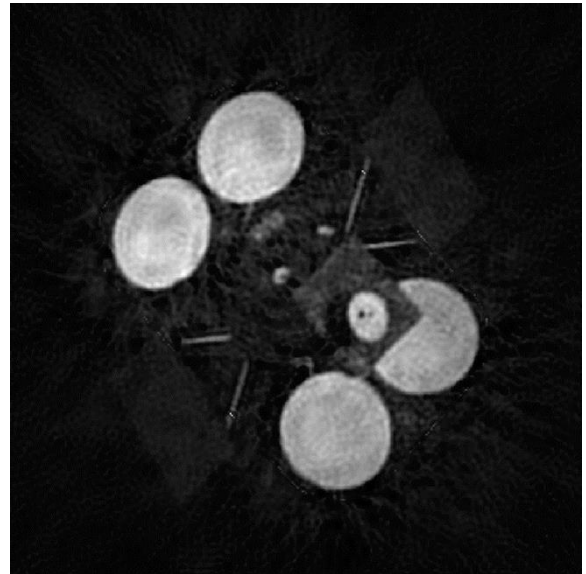
(a)



(b)



(c)



(d)

Fig. 9. Satellite. (a) Context camera image of back-illuminated scene, (b) bandlimited camera image, (c) dirty image using a priori phase corrections learned by comparing the data to the true object, and (d) nonlinear reconstruction with no use of a priori knowledge.

6. CONCLUSION

We demonstrated successful reconstructions from data taken with a fiber-coupled interferometer. The experiment and fringe processing produced quality data for the image reconstruction algorithm. The algorithm successfully reconstructed the three different scenes. With the binary pinhole scene, we demonstrated the accuracy by comparing recovered diameters and separations to truth data. With the bar target reconstruction, we demonstrated that we can achieve a near-theoretical resolution. Additionally, the result for the satellite scene illustrated successful data collections and processing for a realistic geostationary satellite object.

7. REFERENCES

- [1] Goodman, J. W., Statistical Optics, Second Edition, John Wiley & Sons, Inc., Hoboken, NJ (2015).
- [2] Thurman, S. T., and Fienup, J. R., "Fizeau Fourier transform imaging spectroscopy: missing data reconstruction," *Opt. Express* 16, 6631-6645 (2008).
- [3] DeSantis, Z. J. and Fienup, J. R. "Support estimation for phase retrieval image reconstruction from sparse-aperture interferometry data," *Proc. SPIE* 8500, Image Reconstruction from Incomplete Data VII (2012); doi: 10.1117/12.929989.
- [4] DeSantis, Z. J. and Fienup, J. R., "Bootstrapping method for support estimation and image reconstruction for interferometric data," in *Imaging and Applied Optics COSI, Computational Imaging through Turbulence and Scattering Media* (2013).
- [5] DeSantis, Z. J., and Fienup, J. R., "Image reconstruction from sparse interferometric data," in *Imaging and Applied Optics 2014, OSA Technical Digest (online)* (Optical Society of America, 2014), paper STu2F.4.
- [6] Marchesini, S., He, H., Chapman, H. N., Hau-Riege, S. P., Noy, A., Howells, M. R., Weierstall, U., and Spence, J. C. H., "X-ray image reconstruction from a diffraction pattern alone," *Phys. Rev. B* 68, 140101 (2003).
- [7] Crimmins, T. R., Fienup, J. R., and Thelen, B. J., "Improved bounds on object support from autocorrelation support and application to phase retrieval," *J. Opt. Soc. Am. A* 7, 3-13 (1990).
- [8] Fienup, J. R., Crimmins, T. R., Holsztynski, W., "Reconstruction of the support of an object from the support of its autocorrelation," *J. Opt. Soc. Am.* 72, 610-624 (1982).